Exchange biasing of single-domain Ni nanoparticles spontaneously grown in an antiferromagnetic MnO matrix

Daniel P Shoemaker, Madeleine Grossman and Ram Seshadri

Materials Department, Materials Research Laboratory, University of California,
Santa Barbara, CA 93106, USA
and
Department of Chemistry and Biochemistry, Materials Research Laboratory, University of
California, Santa Barbara, CA 93106, USA

E-mail: dshoe@mrl.ucsb.edu

Abstract

Exchange biased composites of ferromagnetic single-domain Ni nanoparticles embedded within and on the surface of large grains of MnO have been prepared by the reduction of $Ni_xMn_{3-x}O_4$ monoliths in flowing 5% H_2/N_2. The Ni precipitates are 20–30 nm in extent, and the majority are completely encased within MnO. The manner in which the Ni nanoparticles are spontaneously formed—starting from a single homogeneous phase—ensures a high degree of dispersion of the Ni and large Ni/MnO interface/volume ratios. The interfaces between ferromagnetic Ni and antiferromagnetic MnO result in magnetic exchange bias below the Néel temperature of MnO. A threefold change in exchange bias fields (from 40 to 120 Oe at 5 K) is observed, depending on the starting Ni content x in the precursor $Ni_xMn_{3-x}O_4$, with smaller x values—fewer or smaller Ni nanoparticles—resulting in larger exchange fields. The exchange bias leads to significant hardening of the magnetization, with coercive fields scaling nearly linearly with the exchange field. The strategies outlined here suggest new and simple routes for creating highly interfacial, functional biphasic composites of nanoparticles embedded within or supported on an oxide matrix.

1. Introduction

Exchange anisotropy, or exchange bias, is a phenomenon occurring at the interfaces between ferromagnetic and antiferromagnetic domains which results in shifting and broadening of magnetic hysteresis loops. Exchange bias is believed to result from the interaction of ferromagnetic (FM) spins with uncompensated antiferromagnetic (AFM) spins at the FM/AFM interface [1–3]. Since its discovery in partially oxidized Co/CoO nanoparticles by Meiklejohn and Bean [4], exchange bias has been observed and engineered in core–shell nanoparticles [5], thin films [6], and granular composites [7]. These architectures are utilized because a high proportion of FM spins must be interfacial in order for exchange bias at the interface to appreciably affect the FM coercivity. While they achieve a high interface/volume ratio, core–shell nanoparticles and thin film architectures are difficult to process in large volumes. Many different methods of processing granular exchange biased systems have been explored, including co-evaporation [8], mechanical milling [9], and spontaneous phase separation [10].

We present a simple route to exchange biased composites of ferromagnets and antiferromagnets via hydrogen reduction of ternary transition metal oxides. Similar methods have been shown to be rapid, reliable, and widely applicable for the production of biphasic [11–14] materials. We have recently established the efficacy of such reductions in the creation of mesoporous materials, obtaining dramatic results such as crystallographically aligned pores in cases where the final porous product and the starting dense monoliths share a common oxygen sublattice [15–17]. The processes are effectively scale independent, and the resulting microstructures can be utilized for nearly any application requiring granular composite materials or supported nanoparticles; in catalysis,

for tailoring mechanical properties, for charge trapping, and in exploring and utilizing interfacial magnetic phenomena. The composites are typically mechanically robust, with porosity that can be induced by reduction of either or both metal species. The requirements for the magnetic exchange processes described in this work are similar to the requirements in other applications, namely chemically pure and monodisperse nanoparticles, sharp interfaces between the two phases, a self-limiting precipitation process, and scalability.

Initial reports from Sort *et al* [14] have demonstrated hydrogen reduction of $Fe_{0.2}Cr_{1.8}O_3$ as a means to obtain metal/oxide composite grains. Only Fe is reduced in this system resulting in nanosized Fe particles within micron sized Cr_2O_3 grains. Interaction between the $\sim$10 nm Fe precipitates and the bulk Cr_2O_3 provides exchange bias fields of 10 Oe. Reduction kinetics of the system $CoCr_2O_4$–Co_3O_4 have been reported by Bracconi and Dufour [18], and Kumar and Mandal [19] have produced Co/Cr_2O_3 composites directly from nitrate precursors.

Here we report on reduction by 5% H_2/N_2 of the system $Ni_xMn_{3-x}O_4$ as a means to obtain Ni/MnO composites with striking nanostructures that are associated with substantial exchange biasing, observed below the Néel temperature of MnO ($T_N = 119$ K). An analysis of the sizes of particles on the surface and in the interiors of the final monoliths reveals that the methods reported here produce Ni nanoparticles with diameters between 20 and 30 nm. Trends are evident relating the Ni content of the precursor spinel (x) to the exchange biasing behavior of the composite. The coercive field of ferromagnetic Ni is dramatically increased as a result of the exchange biasing.

2. Experimental details

Single-phase ceramic oxide monoliths of $Ni_xMn_{3-x}O_4$ were prepared by the decomposition of oxalates as previously reported by Wickham [20]. Oxalates are versatile precursors for mixed metal oxides, and have found extensive use by us in recent years in producing substituted binary [21, 22] and ternary [15, 16, 23] compounds. Stoichiometric amounts of nickel acetate and manganese acetate ($Ni(CH_2COOH)_2 \cdot 4H_2O$ and $Mn(CH_2COOH)_2 \cdot 4H_2O$, Aldrich 99%) were added to a solution containing one equivalent of glacial acetic acid. Excess oxalic acid monohydrate ($H_2(C_2O_4) \cdot H_2O$, Fisher 99.9%) was mixed in a separate solution and both were stirred at 90 °C. Addition of the oxalic acid solution to the dissolved acetates results in co-precipitation of very fine, single-phase nickel–manganese oxalates in which the metals are mixed on the atomic scale. The oxalate powders, $Ni_xMn_{3-x}(C_2O_4)_3 \cdot 2H_2O$, were washed with deionized water and dried at 90 °C, calcined in alumina boats in air at temperatures ranging from 780 to 1200 °C for 10 h, and then quenched into water to prevent conversion to α-Mn_2O_3 or to $NiMnO_3$. The resulting single-phase $Ni_xMn_{3-x}O_4$ spinel powder was pressed into pellets at 100 MPa and sintered at 1325 °C for 24 h, then annealed at the previous calcination temperature and water-quenched.

Reductions were performed in alumina boats in a tube furnace under 5% H_2/N_2 with a flow rate of $\sim$30 sccm. Once the gas mixture had equilibrated, the specimens, as pellets, were heated at 2 °C min^{-1} to 650, 700, or 725 °C, held for 2 h, then cooled at 10 °C min^{-1} to room temperature. Reduced samples were verified to be Ni/MnO by means of x-ray diffraction (XRD, Philips X'Pert with Cu Kα radiation) and Rietveld refinement using the XND program [24]. Thermogravimetric analysis (TGA, Cahn TG-2141), scanning electron microscopy (SEM, FEI Sirion XL40), focused ion beam milling and microscopy (FIB, FEI DB235), and SQUID magnetometry (Quantum Design MPMS 5XL) were used in the various stages of the work reported here.

3. Results and discussion

3.1. The precursor $Ni_xMn_{3-x}O_4$ oxides

Calcination of the single-phase Ni/Mn oxalates results in single-phase cubic and tetragonal spinel compounds, in agreement with the phase diagram reported by Wickham [20]. In their high-temperature state, samples of $Ni_xMn_{3-x}O_4$ with x between 0.15 and 1.00 are reported to be cubic spinels before decomposing into $NiMnO_3$ and α-Mn_2O_3 in the temperature range of 705–1000 °C [20]. Upon quenching in water, samples prepared with $x < 1$ and fired at $\geqslant$1000 °C transform from the high-temperature cubic spinel into single-phase hausmannite-type tetragonal spinel in space group $I4_1/amd$. Slow cooling, air-quenching, or quenching in flowing nitrogen are not rapid enough to prevent decomposition of the solid solution.

Rietveld refinement of the room temperature XRD pattern for the water-quenched compound $Ni_{0.3}Mn_{2.7}O_4$ is shown in figure 1(a). Only peaks for the hausmannite-type solid solution are evident. The single-phase nature of this material is essential for the final reduced composite to possess a homogeneous distribution of Ni precipitates. The refinement assumes a 'normal' spinel, where Ni^{2+} and Mn^{2+} occupy the 4b tetrahedral sites. Mn^{3+} in the 8c octahedral sites induces a cooperative Jahn–Teller distortion which leads to a loss of cubic symmetry [25]. An accurate determination of the cation distribution may be obtained from neutron diffraction and has been investigated by Larson *et al* [26]. When sintered at 1325 °C, samples with x near 1 partially decompose into mixtures of NiO and $Ni_{1-\delta}Mn_{2+\delta}O_4$ as described by Wickham [20], but subsequent annealing at 800 °C for 72 h ensures a return to single-phase tetragonal spinel. Scanning electron micrographs of the dense spinel precursors are shown in figure 2. It is seen that the samples are densely sintered and completely homogeneous. The grain sizes are in the tens of μm. We present these images as a record of the single-phase sample morphology of the spinels before reduction.

3.2. Reduction to Ni/MnO composites

It is imperative in this study to determine the extent of phase separation in Ni/MnO nanocomposites. If reduction of Ni^{2+} to fcc-Ni is not complete, the precipitates would consist of (Ni, Mn)O, which could result in a broader Néel temperatures for the rocksalt and as imperfections at the FM–AFM interface.
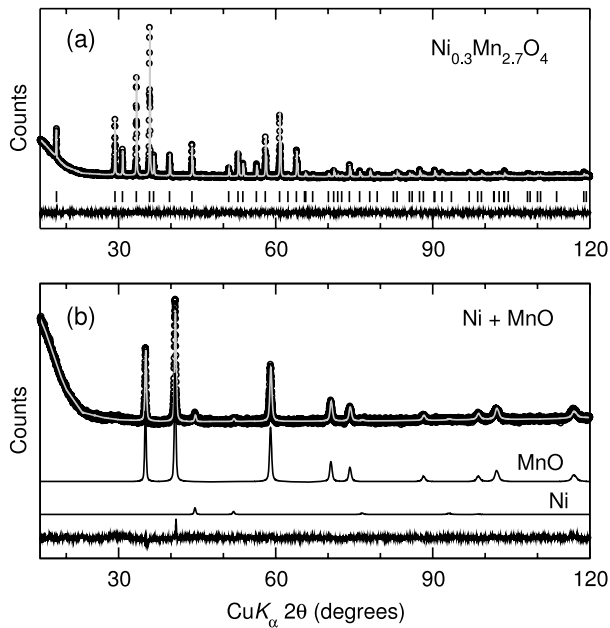
Figure 1. X-ray diffraction Rietveld refinements of (a) $Ni_{0.3}Mn_{2.7}O_4$ single-phase tetragonal spinel (hausmannite) precursor, and (b) the two-phase fcc-Ni/rocksalt MnO composite produced by reduction of the above spinel in 5% H_2/N_2.
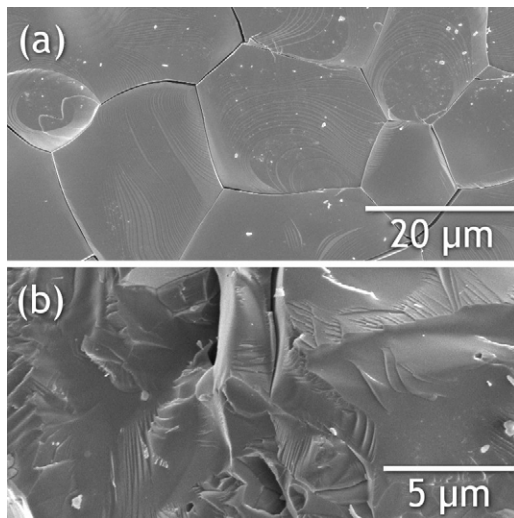

Figure 2. Representative scanning electron microscope images: (a) the as-sintered surface of a dense pellet of $Ni_xMn_{3-x}O_4$ with $x = 0.3$, and (b) the fractured surface of dense pellet with $x = 0.6$. Phase homogeneity is required to ensure an even distribution of precipitates in the final product.

A sharp interface is desired, not only for our investigation of exchange bias, but also for the vast majority of applications of such supported nanoparticle composites. To that end, we have utilized a variety of techniques to verify that Ni^{2+} has been completely reduced, and that NiO or alloyed oxide phases are completely absent within the resolution of our experiments.

Thermogravimetric analysis (TGA) was used to monitor the mass loss of samples upon programmed heating in 5% H_2/N_2. In all cases, TGA confirms that the mass of oxygen
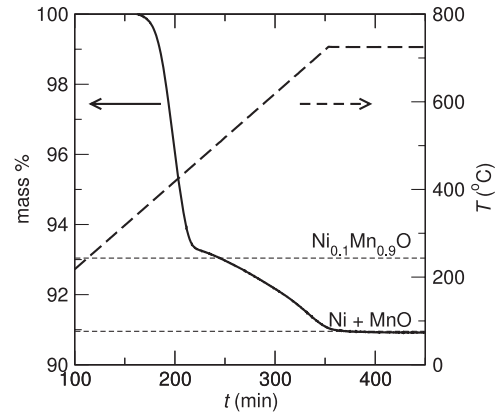

Figure 3. Sample mass (solid) and temperature (dotted) during TGA reduction in 5% H_2/N_2 for $Ni_{0.3}Mn_{2.7}O_4$ shows that reduction proceeds via the formation of an intermediate rocksalt $Ni_{0.1}Mn_{0.9}O$ solid solution, followed by final reduction to metallic Ni. Manganese is not reduced beyond Mn^{2+}.

lost from the sample corresponds to complete reduction of Mn^{3+} to Mn^{2+} and precipitation of metallic nickel (and thus the stoichiometry of the precursor spinel). A TGA weight loss trace for $Ni_{0.3}Mn_{2.7}O_4$ is shown in figure 3 and is consistent with single-phase spinel first quickly reducing to a rocksalt $(Ni_{0.1}, Mn_{0.9})O$ solid solution, followed by precipitation of metallic Ni. The oxidation state of manganese does not decrease below 2+.

This interpretation of the TGA data is verified by Rietveld refinement of XRD data. Analysis of the final composite obtained after reduction in 5% H_2/N_2 indicates only rocksalt MnO and face-centered cubic Ni (figure 1(b)). The question that must be answered is whether Ni has been completely reduced out of the (Ni, Mn)O solid solution. High-spin Mn^{2+} in octahedral coordination has an ionic radius of 0.83 Å, while octahedral Ni^{2+} has a radius of only 0.69 Å [27]. Consequently, when Ni^{2+} enters the MnO lattice, there is significant shrinkage of the cell parameter, which is used in conjunction with TGA to estimate the degree of conversion of the starting phases into pure Ni/MnO. The MnO lattice parameter obtained from Rietveld refinement is plotted in figure 4(a) as a function of the Ni content in the single-phase hausmannite/spinel precursor. The cell parameter of pure MnO, 4.444 Å, is indicated as a horizontal dashed line.

It is evident from figure 4(a) that for low substitution of Ni (x in the starting phases) the reduction temperature must be increased from 650 to 725 °C to ensure complete reduction and avoid rocksalt (Ni, Mn)O solid solution. Depression of the required reduction temperature of $Ni_xMn_{3-x}O_4$ as x deviates from Mn_3O_4 is a consequence of the higher ionization energy of Ni^{2+}. In other words, more energy is released by reduction of Ni^{2+} ions than by that of Mn^{2+}, so the reduction to metal occurs more readily when x is larger. The greater ease of reduction of Ni over Mn is suggested by the appropriate Ellingham diagram [28]. In addition to XRD and TGA, the saturation magnetization M_S of the magnetic Ni nanoparticle precipitates can be used to determine the completeness of Ni reduction. The convergence of a_{MnO}
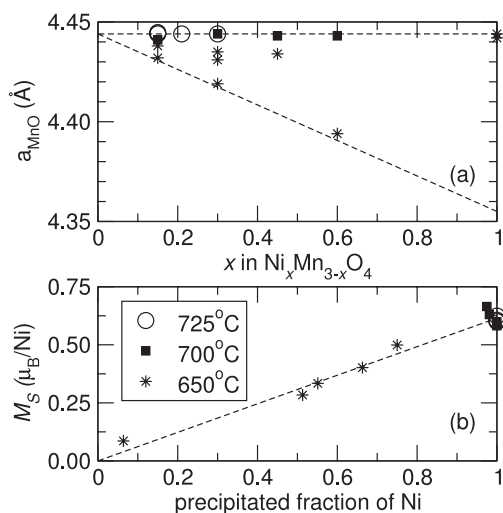
Figure 4. (a) Lattice parameter of MnO obtained by Rietveld refinement of samples after hydrogen reduction at varying temperatures. The diagonal dotted line is the calculated lattice parameter of a (Ni, Mn)O solid solution, while the top line represents the desired conversion to pure MnO. (b) Magnetic saturation of reduced Ni/MnO samples increases linearly with the completeness of Ni reduction as determined by a_{MnO} from Rietveld refinement, and reaches the value associated with bulk Ni metal of $M_S \approx 0.6 \ \mu_B/Ni$.

Figure 5. Representative scanning electron microscope images: (a) the as-reduced surface of a composite with precursor Ni content $x = 0.15$ appears unchanged at low magnification, as grain size is unchanged. At higher magnification (b), mesopores and precipitates become evident. At still higher magnification (c), the surface of the composite is seen to be dominated by small faceted faces and nanopores, accompanied by lighter-colored Ni nanoparticles which are tens of nanometers in diameter.

and M_S to their respective theoretical values of 4.444 Å and 0.6 μ_B/Ni for a completely reduced xNi/MnO composite is shown in figure 4(b). It is apparent that these methods of characterization are complementary, regardless of Ni content x.

3.3. Morphology of the reduced composites

Hydrogen reduction of single-phase oxide monoliths can lead to striking hierarchically porous microstructures, which have been characterized by Toberer *et al* [15–17]. At first glance, low-magnification SEM micrographs of $Ni_x Mn_{3-x} O_4$ precursor spinels (figure 2) and Ni/MnO reduced samples (figures 5(a) and 6(a)) appear unchanged. However, higher magnification (figures 5(b), (c) and 6(b)–(e)) reveals that reduced composites contain aligned pores in rocksalt MnO covered with Ni metal nanoprecipitates approximately 25 nm in diameter. The particles seen in SEM are determined to be Ni based upon observation with backscattering SEM, Scherrer broadening from XRD, agreement of the volume fraction seen in FIB cross-sections, and magnetic saturation that corresponds to 0.6 μ_B/Ni. These data, combined with XRD Rietveld and TGA analysis, give a thorough characterization of the composites. Transmission electron microscopy investigation is being conducted to investigate the nature of the Ni/MnO interface, and the orientation of embedded nanoparticles with respect to the matrix.

It has been previously suggested [15, 17] that the common close-packed oxide sublattice of spinel and rocksalt allows the transformation from one to the other to proceed without extensive reconstruction. Porosity is introduced during the spinel to rocksalt transformation while leaving the oxygen framework lar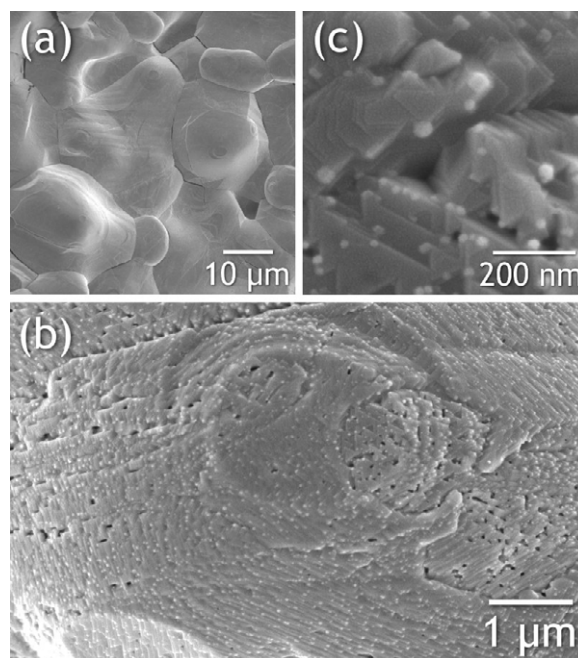gely intact. A reconstructive phase transformation is avoided as cations travel only small distances, of the order of the mesopore diameter. The associated volume loss produces a pore structure that can be regarded as negative crystals—voids in crystals that possess the same facets as the crystals themselves.

Although the pores are as small as 20 nm, the pore and surface edges are aligned at right angles over the entire breadth of the 20 μm grains. This long-range alignment implies that the MnO grains observed in SEM are in fact single crystals with the same orientation and extent as the pre-reduction spinel grains [15, 16]. Increasing the reduction temperatures leads to densification and closing of the pores in the MnO monolith. However, in the interest of maintaining small Ni nanoparticles (and thus a high interface/volume ratio), and because the majority of nanoparticles are completely encased in MnO even in porous samples, reduction was performed at the lowest temperature that allowed complete Ni precipitation.

If we assume that, for the different values of x, the number of nuclei are the same, and that increasing x only affects the growth (i.e. the diameter) of the particles, then we would expect only a weak dependence (changing as $x^{\frac{1}{3}}$) of the particle diameter rate on x. If we assume that increasing x also increases the number of Ni nuclei upon reduction, then average particle diameter would show an even weaker dependence on x. We have analyzed the Ni particles in the SEM images of the surfaces of the monoliths by using the program IMAGEJ [29] to prepare histograms of particle size distributions. These are plotted in figure 7 for the different monoliths. It is seen that
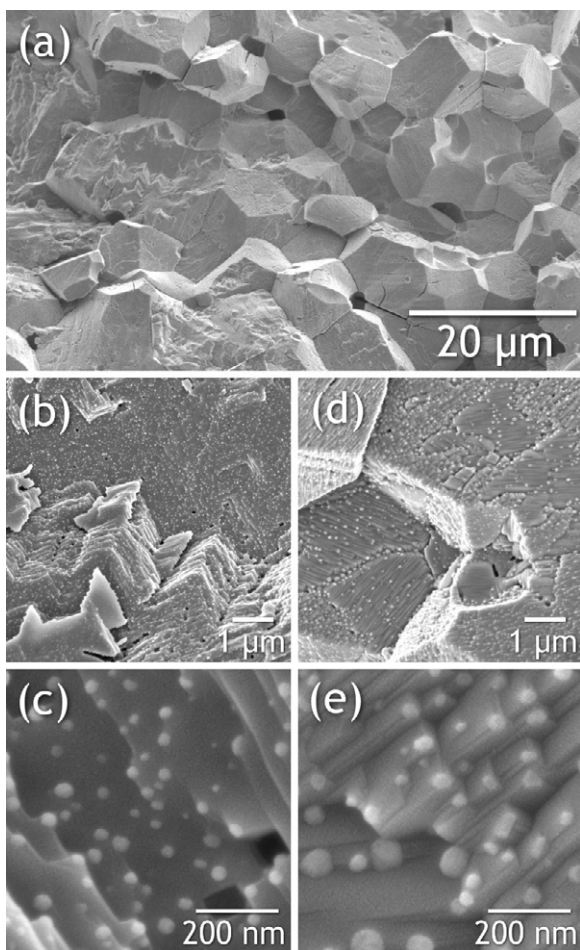
Figure 6. Representative scanning electron microscope images: (a) the fractured surface of the composite obtained from reducing a dense pellet of $Ni_xMn_{3-x}O_4$ with $x = 0.3$ at $725\,°C$ for 2 h. An intragrain fracture is shown in (b) and (c), where the Ni nanoparticles appear as light spots on the darker MnO matrix. Faceting is often seen to extend across the entire grains. An intergrain fracture surface is magnified in (d) and (e).

Figure 7. The mean diameters of the Ni particles on the surface of the MnO matrix as a function of the initial Ni content x in $Ni_xMn_{3-x}O_4$. Error bars indicate one standard deviation in the particle diameter. Typically at least 30 distinct particles were counted in preparing the distributions. Up to $x = 0.45$, the sizes are clustered around 30 nm and seem to not depend strongly on x.

Figure 8. It is apparent that on the exposed surface of a reduced sample ($700\,°C$, 2 h) of $Ni_xMn_{3-x}O_4$ with $x = 0.45$, the Ni particle size is strongly dependent on the underlying MnO environment. The triangular faces upper right, assumed to be {111} facets, support large, sparse nuclei. The square faces bottom left, most likely {100} or {110}, are covered in a higher density of smaller Ni particles.

mean particle diameters range from ∼15 to 35 nm, but given the distribution of particle sizes, an increase in particle size with starting x cannot be ascertained until a nickel content of $x = 0.60$ is reached.

Indeed, a clearer correlation is found for Ni particle size with the specific crystallographic face of MnO upon which it grows than with the starting x value. It is evident in figure 8 of an $x = 0.45$ specimen that regions can be found which exhibit a wide variety of surface particle sizes and spacings depending on the nucleation environment. The coherent pore structure introduced by reduction produces square or triangular facets, seen in figure 9(a), which correspond to exposed {100} or {111} faces.

Cross-sections of reduced grains produced by FIB milling, shown in figure 9, reveal that the bulk MnO contains Ni nanoparticles of similar dimensions to those on the surface. Porosity is still prevalent in the bulk of the monolith as it is on the monolith surface. This is necessary to accommodate the volume loss of the structure while retaining the size and alignment of the MnO grains. Interestingly, the Ni particle
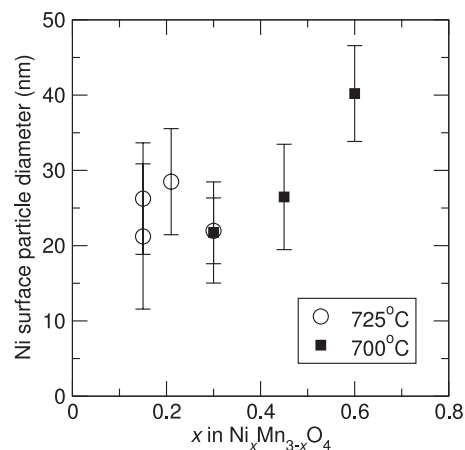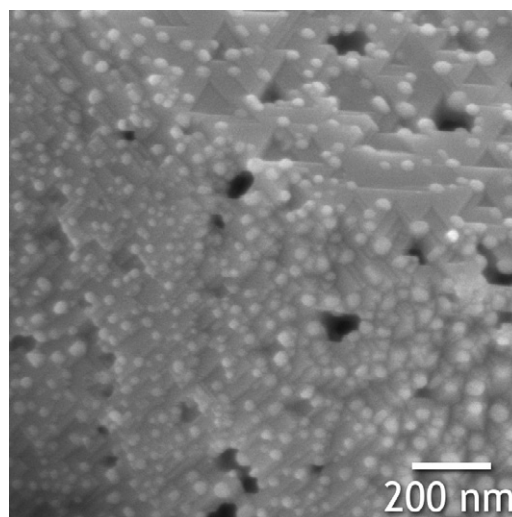
size in an $x = 0.6$ composite (figure 9(a)) appears to be much larger than when $x = 0.15$ (figure 9(b)), while the Ni size as judged by SEM surface analysis did not reveal such a significant difference.

By a comparison of lattice parameters, and assuming no sintering during reduction, the fraction of intragranular porosity produced by the conversion of $Ni_xMn_{3-x}O_4$ to xNi/MnO increases linearly from 16% when $x = 0$ to 39% when $x = 0.6$, which is in rough agreement with observations of the intragranular pore volume in FIB-milled samples. Many Ni nanoparticles observed in cross-section (figure 9) are completely encased within the MnO matrix. On the basis of the observed surface density of Ni particles and
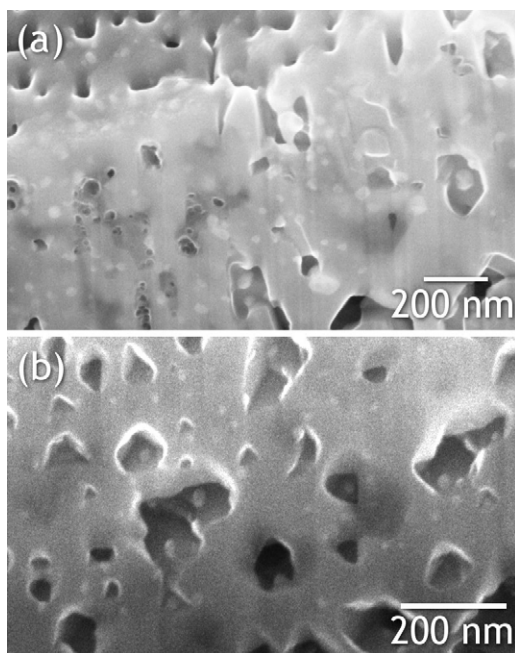
Figure 9. FIB cross-sections of reduced composites show that a large proportion of Ni nanoparticles are completely encased within the MnO matrix. In (a), a sample with Ni content $x = 0.6$ has much larger light-colored Ni precipitates within the bulk. The rounded area upper left is the unmilled surface of the composite. In (b), a sample with $x = 0.15$ contains noticeably smaller Ni particles.

assuming 100 nm diameter pores, it can be determined that the observed surface Ni particles only constitute about 20% of the volume of Ni that must be precipitated. Therefore, we estimate that approximately 80% of the Ni grains are encased within the MnO matrix. Such a high proportion implies that Ni particle interfaces will predominantly be particle–matrix as desired, rather than particle–void.

3.4. Magnetic behavior

The observation of magnetic exchange bias in our samples is an indication of the suitability of the hydrogen reduction process for producing nanostructured materials that exhibit chemically and structurally sharp interfaces, while maintaining large interfacial areas and intimate contact between the two phases. Magnetic studies of the composites reveal unambiguously the presence of significant loop shifting and broadening as a result of field-cooling below the MnO Néel temperature.

The magnetic behavior of the reduced samples, including evidence for exchange bias, was studied by recording M–H traces after field-cooling under a 50 kOe field: M was measured as a function of decreasing H (going from 50 to -50 kOe) and then the loop was closed by measuring back to 50 kOe. The hysteresis loop (figure 10) for an $x = 0.3$ sample at 300 and at 150 K is narrow and centered around $H = 0$, as would be expected above T_N. At 5 K, the hysteresis loop is broadened significantly, and field-cooling ($H = 50$ kOe) results in a loop that is displaced by the exchange field $-H_E$. The most convincing evidence for exchange bias lies in the dependence of field-cooled H_E as a function of temperature.
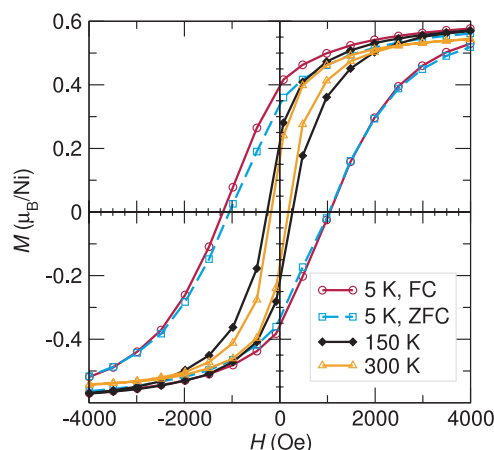

Figure 10. Magnetization M as a function of magnetic field H for a Ni/MnO composite with $x = 0.3$ at different temperatures and cooling fields. At 150 and 300 K, the hysteresis loop remains centered about the origin and there is minimal difference between the field-cooled (FC) and the zero-field-cooled (ZFC) loops. For hysteresis loops at 5 K, well below T_N, measurement after field-cooling with $H = 50$ kOe results in a loop that is broader and shifted along $-H_E$ in relation to the zero-field-cooled (ZFC) loop.

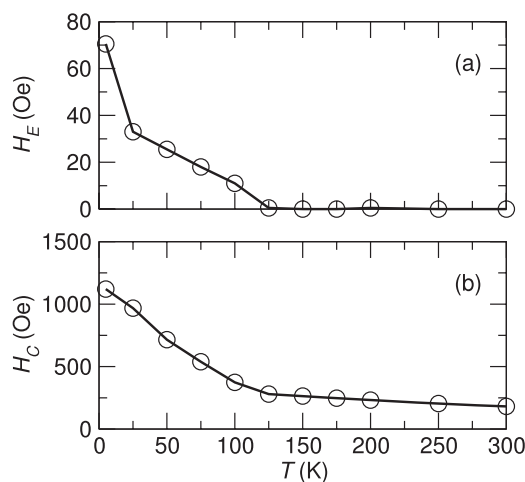(This figure is in colour only in the electronic version)

Figure 11. Temperature dependence of (a) exchange field H_E and (b) coercive field H_C for an $x = 0.3$ sample after field-cooling at 50 kOe. Both quantities display a marked increase upon cooling below the Néel temperature of MnO, $T_N = 119$ K. This onset of broadening and loop shift below T_N is one indication of exchange bias in the composite. Error is smaller than data markers in each case.

Both the coercivity and exchange field data in figure 11 reveal a sharp increase upon cooling below $T_N = 119$ K; H_E is zero above T_N.

Exchange bias effects in nanostructures are distinct from many established thin film models for a number of reasons: the FM particles can be single domain, and can be encased within a single domain of AFM; the spin orientation with respect to the interface approaches a random distribution as the particles become more spherical; and field cannot necessarily be applied in an easily determined crystallographic direction.
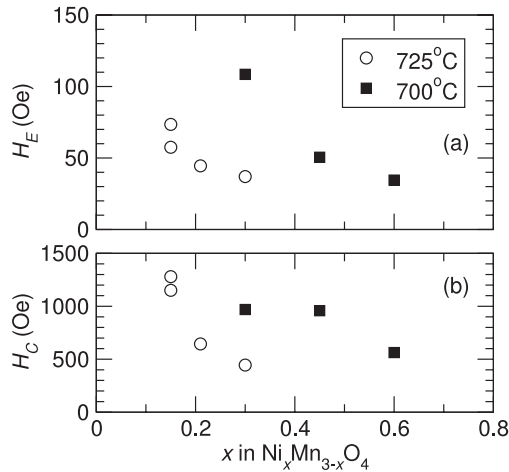
Figure 12. (a) Exchange bias field H_E and (b) coercive field H_C at 5 K as a function of the initial Ni content x in the reduced Ni/MnO composites. Data were obtained after field-cooling under a 50 kOe field. The exchange field of the Ni nanoparticles decreases with Ni content for each firing temperature (indicated in the figure) in response to either the decreasing amount of interface or a higher density of Ni particles which interrupt the extent of antiferromagnetic MnO domains. Similarly, the coercive field decreases with increasing Ni content in the oxide precursor.

The spins in MnO are arranged in the {111} plane along $\langle 11\bar{2} \rangle$ [30], but if we consider that round Ni particles are embedded within them, the interface may consist of a very complex configuration of compensated and uncompensated spins. Without knowledge of this detailed magnetic structure, a few conclusions can be reached. The magnetocrystalline anisotropy of MnO is not large compared to many common AFM oxides [31], so a substantial amount of reorientation of uncompensated interfacial spins may be expected upon Ni spin reversal. This uncompensated 'spin dragging' and the decrease in thermal energy heightens the energy barrier required to reverse the spins, which is the main cause of the H_C increase as the composite is cooled below T_N [3, 32, 33]. This substantial coercivity enhancement at low temperatures is aided by the random nature of the Ni/MnO interface, and can be differentiated from the case where compensated AFM spins possess stronger magnetocrystalline anisotropy below T_N. Such composites exhibit a peak in H_C around T_N, implying that the AFM spins do not reverse with applied field at lower temperature [34, 35]. In our samples, coercivity broadening upon cooling is accompanied by increasing H_E as a larger proportion of MnO spins become pinned in the orientation of field-cooling, resulting in the unidirectional anisotropy that is most commonly associated with exchange bias [36].

Figure 12(a) shows that as the nickel content x increases, H_E decreases significantly for samples reduced at either 700 or 725 °C. At both reduction temperatures, the highest H_E is found for the smallest x, and the smallest H_E is found for the largest x. The coercive field H_C shows similar behavior, as seen from figure 12(b). Increasing the reduction temperature for samples with $x = 0.30$ results in decreased exchange bias, which is contrary to the finding that a wider, chemically diffuse interface leads to higher coercivity, as described by Ohldag,
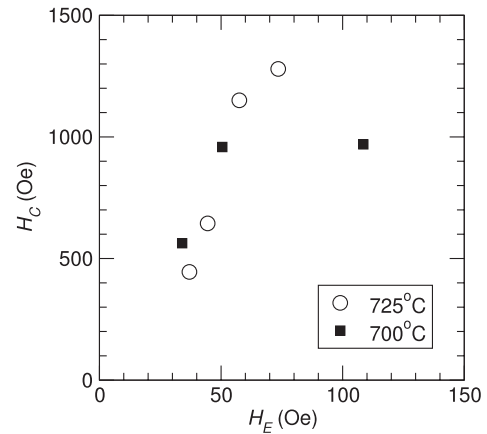

Figure 13. Coercive field as a function of exchange field at 5 K for the different Ni/MnO composites. For most of the composite systems, H_C varies nearly linearly with H_E.

et al [32]. This disagreement merits further investigation and is not necessarily due to purely magnetic phenomena, but could be the result of subtle microstructural changes, such as particle growth or pore closure.

The exchange behavior can be influenced by many of these factors, including Ni particle size, shape, and spacing, crystallinity and purity of both phases, and the amount, thickness, and orientation of the Ni/MnO interface. In our study, let us assume that the only parameters which vary appreciably with the Ni content x are the spacings between Ni particles and their size. The two limits of this dependence are the cases where either Ni particle diameter d_{FM} or the total number of Ni particles remains unchanged. In the first case, the volume of MnO around each Ni particle would decrease as $V_{AFM} \propto x^{-1}$, while in the second case, the Ni diameter would increase as $d_{FM} \propto x^{1/3}$. In exchange biased nanostructures of spherical FM particles in an antiferromagnetic matrix, the strength of the exchange field H_E has been suggested to vary as $H_E \propto d_{FM}^{-1}$, where d_{FM} is the diameter of the FM particle [7, 37]. By following this model for an interfacial effect, we anticipate that the exchange field H_E should decrease with increasing ferromagnetic particle size. For the case where only the Ni diameter changes, we expect the relation $H_E \propto x^{-1/3}$. With the current data, we are unable to fit the dependence of H_E on x to either one or the other model. Another possibility to consider is that with increasing numbers of the Ni nanoparticles, the sizes of the antiferromagnetic MnO domains will be decreased, and this too, may influence the extent of exchange bias. This last possibility has not been examined on the length scales at hand in existing models of exchange bias.

In figure 13 we plot the coercivity at 5 K as a function of the exchange field for the different systems measured, data for which are displayed in figure 12. We see that the coercivity varies nearly linearly with the exchange field, with the exception of one outlier. Given the inherent complexity of granular exchange biased systems, we assert only that the linear relation between coercivity and exchange is simply an indication of increasing interfacial area between the two

magnetic components, and uniformity in the mechanisms of exchange bias as described above.

4. Conclusions

We have demonstrated that hydrogen reduction of $Ni_xMn_{3-x}O_4$ spinels produces Ni/MnO composites with significant interfacial area between antiferromagnetic MnO and ferromagnetic Ni, and associated exchange bias. With increasing nickel content x, these effects weaken, possibly because of a decrease in the relative proportion of interfacial spins in the composite. Exchange bias effects at the FM–AFM interface lead to an increase in H_C. A nearly linear relationship is found between H_C and H_E in these systems, and in the samples displaying the greatest degree of exchange biasing at 5 K, the coercive field is enhanced nearly threefold. This work also points the way to other applications where granular or supported nanoparticle structures with clean interfaces and high interfacial areas are required.

Acknowledgments

References

[1] Blamire M and Hickey B 2006 Magnetic materials: compensating for bias *Nat. Mater.* **5** 87–8
[2] Kuch W, Chelaru L I, Offi F, Wang J, Kotsugi M and Kirschner J 2006 Tuning the magnetic coupling across ultrathin antiferromagnetic films by controlling atomic-scale roughness *Nat. Mater.* **5** 128–33
[3] Nogués J and Schuller I K 1999 *J. Magn. Magn. Mater.* **192** 203–32
[4] Meiklejohn W H and Bean C P 1957 New magnetic anisotropy *Phys. Rev.* **105** 904–13
[5] Skumryev V, Stoyanov S, Zhang Y, Hadjipanayis G, Givord D and Nogués J 2003 Beating the superparamagnetic limit with exchange bias *Nature* **423** 850–3
[6] Fitzsimmons M R, Bader S D, Borchers J A, Felcher G P, Furdyna J K, Hoffmann A, Kortright J B, Schuller I K, Schulthess T C, Sinha S K, Toney M F, Weller D and Wolf S 2004 Neutron scattering studies of nanomagnetism and artificially structured materials *J. Magn. Magn. Mater.* **271** 103–46
[7] Nogués J, Sort J, Langlais V, Skumryev V, Suriñach S, Muñoz J S and Baró M D 2005 Exchange bias in nanostructures *Phys. Rep.* **422** 65–117
[8] Yi J-Y, Hirata G A and Rudee M L 2001 Microstructure and magnetic properties of Co–CoO nanocomposite films *Mater. Res. Soc. Symp. Proc.* **674** T3.4.1
[9] Sort J, Nogués J, Amils X, Suriñach S, Muñoz J S and Baró M D 1999 Room-temperature coercivity enhancement in mechanically alloyed antiferromagnetic–ferromagnetic powders *Appl. Phys. Lett.* **75** 3177–9
[10] Narita K, Koga S and Motowaki Y 1981 Displaced hysteresis loop of Cu–Mn–Al alloy *J. Appl. Phys.* **52** 5751–5
[11] Laurent Ch, Demai J J, Rousset A, Kannan K R and Rao C N R 1994 Fe–Cr/Al₂O₃ metal–ceramic composites: nature and size of the metal particles formed during hydrogen reduction *J. Mater. Res.* **9** 229–35
[12] Suenaga S, Suetsuna T, Harada K and Fukasawa T 2004 *In situ* formation of metal nanoparticles on ceramic surface *J. Am. Ceram. Soc.* **87** 963–6
[13] Pecharromán C, Esteban-Cubillo A, Montero I, Moya J S, Aguilar E, Santaren J and Alvarez A 2006 Monodisperse and corrosion-resistant metallic nanoparticles embedded into sepiolite particles for optical and magnetic applications *J. Am. Ceram. Soc.* **89** 3043–9
[14] Sort J, Langlais V, Doppiu S, Dieny B, Suriñach S, Muñoz J S, Baró M D, Laurent Ch and Nogués J 2004 Exchange bias effects in Fe nanoparticles embedded in an antiferromagnetic Cr₂O₃ matrix *Nanotechnology* **15** S211–4
[15] Toberer E S and Seshadri R 2005 Spontaneous formation of macroporous monoliths of mesoporous manganese oxide crystals *Adv. Mater.* **17** 2244–6
[16] Toberer E S, Lofvander J P and Seshadri R 2006 Topochemical formation of mesoporous MnO crystals *Chem. Mater.* **18** 1047–52
[17] Toberer E S, Grossman M, Schladt T, Lange F F and Seshadri R 2007 Epitaxial manganese oxide thin films with connected porosity: topotactic induction of crystallographic pore alignment *Chem. Mater.* **19** 4833–8
[18] Bracconi P and Dufour L C 1975 Hydrogen reduction of cobalt–chromium spinel oxides. II. Cobalt chromite (CoCr₂O₄)–cobalt oxide (Co₃O₄) solid solutions *J. Phys. Chem.* **79** 2400–5
[19] Anil Kumar P and Mandal K 2007 Exchange bias in Co–Cr₂O₃ nanocomposites *J. Appl. Phys.* **101** 113906
[20] Wickham D G 1964 Solid-phase equilibria in the system NiO–Mn₂O₃–O *J. Inorg. Nucl. Chem.* **26** 1369–77
[21] Risbud A S, Spaldin N A, Chen Z Q, Stemmer S and Seshadri R 2003 Magnetism in polycrystalline cobalt-substituted zinc oxide *Phys. Rev.* B **68** 205202
[22] Lawes G, Risbud A S, Ramirez A P and Seshadri R 2005 Absence of ferromagnetism in Co and Mn substituted polycrystalline ZnO *Phys. Rev.* B **71** 045201
[23] Toberer E S, Joshi A and Seshadri R 2005 Template-free routes to macroporous monoliths of nickel and iron oxides: toward porous metals and conformally coated pore walls *Chem. Mater.* **17** 2142–7
[24] Bérar J F and Baldinozzi G 1998 XND code: from x-ray laboratory data to incommensurately modulated phases. Rietveld modelling of complex materials *IUCr-CPD Newslett.* **20** 3–5
[25] Goodenough J B 1998 Jahn–Teller phenomena in solids *Annu. Rev. Mater. Sci.* **28** 1–27
[26] Larson E G, Arnott R J and Wickham D G 1962 Preparation, semiconduction, and low temperature magnetization of the system Ni₁₋ₓMn₂₊ₓO₄ *J. Phys. Chem. Solids* **23** 1771–81
[27] Shannon R D 1976 Revised effective ionic radii and systematic studies of interatomic distances in halides and chalcogenides *Acta Crystallogr.* A **32** 751–67
[28] Smeltzer W W and Young D J 1975 Oxidation properties of transition metals *Prog. Solid State Chem.* **10** 17–54
[29] Abramoff M D, Magelhaes P J and Ram S J 2004 Image processing with ImageJ *Biophotonics Int.* **11** 36–42
[30] Goodwin A L, Tucker M G, Dove M T and Keen D A 2006 Magnetic structure of MnO at 10 K from total neutron scattering data *Phys. Rev. Lett.* **96** 047209
[31] van Lierop J, Schofield M A, Lewis L H and Gambino R J 2003 Exchange bias in a thin film dispersion of MnO nanocrystallites in Co *J. Magn. Magn. Mater.* **264** 146–152
[32] Ohldag H, Regan T J, Stöhr J, Scholl A, Nolting F, Löning J, Stamm C, Anders S and White R L 2001 Spectroscopic identification and direct imaging of interfacial magnetic spins *Phys. Rev. Lett.* **87** 247201

[33] Skumryev V, Stoyanov S, Zhang Y, Hadjipanayis G,
      Givord D and Nogués J 2003 Beating the superparamagnetic
      limit with exchange bias *Nature* **423** 850–3

[34] Hagedorn F B 1967 Exchange anisotropy in oxidized permalloy
      thin films at low temperatures *J. Appl. Phys.* **38** 3641–5

[35] Fulcomer E and Charap S H 1972 Thermal fluctuation
      aftereffect model for some systems with ferromagnetic–
      antiferromagnetic coupling *J. Appl. Phys.* **43** 4190–9

[36] Ohldag H, Scholl A, Nolting F, Arenholz E, Maat S,
      Young A T, Carey M and Stöhr J 2003 Correlation between
      exchange bias and pinned interfacial spins *Phys. Rev. Lett.*
      91 017203

[37] Baltz V, Sort J, Landis S, Rodmacq B and Dieny B 2005
      Tailoring size effects on the exchange bias in
      ferromagnetic–antiferromagnetic <100 nm nanostructures
      Phys. Rev. Lett. **94** 117201–4